Step-by-Step Maturation Mechanism of Binary Toxin Pore Revealed by Cryo-EM Analysis

Tomohito Yamada[1#], Yukihiko Sugita[2,3,4], Toru Yoshida[1,5], Takeshi Noda[2,3], and Hideaki Tsuge[1,6,7#]

1. Faculty of Life Sciences, Kyoto Sangyo University, Kamigamo-motoyama, Kita-ku, Kyoto, 603-8555, Japan
2. Laboratory of Ultrastructural Virology, Institute for Life and Medical Sciences, Kyoto University, 53 Shogoin Kawahara-cho, Sakyo-ku, Kyoto 606-8507, Japan
3. Laboratory of Ultrastructural Virology, Graduate School of Biostudies, Kyoto University, 53 Shogoin Kawahara-cho, Sakyo-ku, Kyoto 606-8507, Japan
4. Hakubi Center for Advanced Research, Kyoto University, 53 Kawahara-cho, Shogoin, Sakyo-ku, Kyoto 606-8507, Japan
5. Department of Chemical and Biological Sciences, Faculty of Science, Japan Women's University, 2-8-1 Mejirodai, Bunkyo-ku, Tokyo, 112-8681, Japan
6. Institute for Protein Dynamics, Kyoto Sangyo University, Kamigamo-motoyama, Kita-ku, Kyoto, 603-8555, Japan
7. Center for Molecular Research in Infectious Diseases, Kyoto Sangyo University, Kamigamo-motoyama, Kita-ku, Kyoto, 603-8555, Japan

#Corresponding authors

Tomohito Yamada, t.mountain.rf23doc@gmail.com

Hideaki Tsuge, tsuge@cc.kyoto-su.ac.jp

Abstract

Membrane pore-forming proteins (PFPs) form ring-shaped membrane-translocating oligomers on membranes, contributing to infection, immunity, and cell death functions. Binary toxins produced by some bacteria consist of an enzymatic component that acts as a toxin and a membrane-binding component that forms a pore that delivers the enzymatic component into target cells. Cryo-electron microscopy (cryo-EM) has advanced our understanding of these translocation mechanisms by revealing several binary toxin complexes' structures. However, the mechanisms underlying the initial pore formation remain unclear. We determined the structures of several oligomeric forms of the membrane-binding component Ib of the Iota toxin from *Clostridium perfringens* at various stages of pore formation. Structural comparisons revealed how the symmetrically arranged soluble oligomer (prepore) asymmetrically mature into a transmembrane oligomer (pore). These findings enhance our understanding of

mechanisms of PFP and provide a structural basis for developing nanodevices using membrane pores.

Significance Statement

Although the mode of action of pore-forming proteins (PFPs) has been increasingly elucidated, the structural mechanisms underlying their maturation into membrane-spanning pores remain elusive. One of the key challenges is the difficulty in capturing the intermediate states between the soluble prepore and the mature pore, and its structural analysis. In this study, we successfully prepared the super-complex formed by a bacterial toxin PFP. The super-complex inhibited the constituting oligomers to maturate into the pore, which enabled structural determination of multiple intermediate state. Comparative structural analysis revealed that the transition from prepore to pore occurs through stepwise, domino-like conformational changes. The analysis workflow and insights from this study are expected to advance the field of PFP research.

53 Membrane pore-forming proteins (PFPs) are a family of proteins produced by many organisms,
54 including bacteria, which form homogeneous or heterogeneous multimeric pores on target
55 biological membranes. These proteins involve various vital functions, including cell death,
56 immunity, and infection[1,2]. PFPs are produced as soluble monomers that form ring-shaped
57 oligomers and subsequently create membrane-spanning α-helices or β-barrels to form pores in
58 various biological membranes. Especially, toxic PFPs are known as pore-forming toxins (PFTs).
59 These PFTs can disrupt the homeostasis of target cells by forming pores, leading to the efflux of
60 ions, amino acids, and water and ultimately inducing cell death.
61
62 *Clostridium perfringens*[3], *Clostridioides difficile*[4], *Clostridium spiroforme*[5],
63 *Clostridium botulinum*[6] and *Bacillus anthracis*[7] produce binary toxins (Iota toxin; Ia and Ib,
64 CDT; CDTa and CDTb, CST; CSTa and CSTb, C2 toxin; C2I and C2II, Anthrax toxin; LF, EF,
65 and PA) composed of enzymatic component and membrane-binding component which function
66 as PFPs[8]. Binary toxins are classified into two groups: intestinal toxins from Clostridium,
67 including the Iota toxin, CDT, CST, and C2 toxin, which have homologous enzymatic
68 components such as actin ADP-ribosyltransferase. The other is the anthrax toxin, whose enzyme
69 components (EF and LF) differ from those of clostridial ADP-ribosyltransferases in both
70 structure and function. However, the membrane-binding components of these toxins are highly
71 conserved, except for their receptor-binding domains. The addition of the enzymatic component
72 alone to cells or organisms does not result in activity, whereas the membrane-binding
73 component alone induces necrosis and dermonecrosis[9,10]. However, components A and B co-
74 addition increases toxicity compared to their individual addition, inducing morphological
75 changes and cell death[11].
76
77 Cell entry mechanisms are similar for clostridial binary toxins and anthrax toxins. The
78 monomeric membrane-binding component binds to the target cell receptor and is activated by
79 proteases to form a soluble ring-shaped oligomer (prepore). The endosomes take up the
80 enzymatic components and prepores. As the endosome acidifies, the pore undergoes a
81 conformational change into a membrane-spanning β-barrel pore, allowing the enzymatic
82 component to translocate into the cell[12,13]. The translocated enzymatic component exerts severe
83 effects on host cells through actin depolymerisation via ADP-ribosylation activity by clostridial
84 binary toxins[6,14,15], or inhibition of signalling pathways through degradation of MAPKK in
85 anthrax toxin[16,17]. At first, it was shown that the pore of anthrax toxin PA forms the narrowest
86 constriction site (ϕ-clamp) with a diameter of only 6 Å in the centre[18,19]. Understanding how the
87 enzymatic component passes through the narrow ϕ-clamp is key interest in studying membrane
88 translocation mechanisms of binary toxins. We previously determined the cryo-electron

89 microscopy (cryo-EM) structures of the enzyme-pore complexes of the iota and CDT toxins[20,21].
90 The constriction sites of Ib and CDTb, as named ϕ-clamp in PA, were conserved among Ib and
91 CDTb. We found that after complex formation with Ca-edge and NSQ-loop, which are
92 constriction-sites of the pore, the N-terminal α-helix of the enzymatic component tilts towards
93 the ϕ-clamp, and this structure further unfolds[20,21]. In the case of anthrax toxin, the first α-helix
94 of LF and EF unfold and dock into a deep amphipathic cleft called the α-clamp[22]. Thus, N-
95 terminal unfolding is commonly observed in clostridial binary toxins and anthrax toxins;
96 however, they use different binding modes. It is hypothesised that the disordered structure
97 passes through the ϕ-clamp and refolds its secondary structure within the β-barrel or cytosol. As
98 described above, binary toxin membrane pores are not only pore-forming toxins but also serve
99 as an intriguing research subject because of their unique translocation mechanism involving the
100 unfolding of the enzymatic component.
101
102 Mutations in the F427 residue forming the ϕ-clamp of the anthrax toxin PA-pore, as
103 well as the surrounding residues, have significant effects on the maturation from prepore to pore
104 and the translocation activity of the enzymatic component[23–25]. In anthrax PA, point mutation of
105 the D425A which is located at two residues upstream of F427, does not affect the
106 oligomerisation ability, but inhibits the conformational change to the pore state. Cryo-EM
107 structural analysis of this mutant revealed that the oligomer was formed by PA protomers in
108 multiple intermediate states between prepore and pore conformations[26]. Furthermore, adjacent
109 protomers have similar structural states, suggesting that maturation from prepores to pores
110 proceeds in a domino-like manner within the heptamer. However, the complete heptamer
111 structure of each intermediate in this domino-like pore maturation process has not yet been
112 experimentally revealed.
113
114 By chance, we obtained a supercomplex in which multiple Ib oligomers were
115 assembled radially (Ib-rosette) while preparing the wild-type Ib component of the iota toxin
116 with liposome. A single particle structural analysis of the Ib-rosette sample revealed that it
117 consisted of both Ib-pores with formed β-barrels and Ib-prepores without the β-barrels. A
118 detailed analysis of the prepore class allowed us to determine the structure of a seven-fold
119 symmetric prepore for the first time in Ib, and multiple asymmetric prepore structures.
120 Comparison with previously reported structures revealed that the protomers forming these
121 prepores were in an intermediate state between the prepore and pore states. Furthermore,
122 comparison of the series of obtained overall structures suggested that the symmetrically
123 arranged protomers underwent a partial loss of symmetry, and this structural change proceeded
124 step-by-step in a domino-like manner to mature into pores. In this paper, we report on the pore

maturation process deduced from comparing multiple prepore structures, and high-resolution pore structure obtained in this study.

Results

Cryo-EM single particle analysis of Ib-rosette

While attempting to prepare Ib-pores reconstituted in liposomes, the obtained sample was observed using negative staining and cryo-EM revealing that the structure consisted of multiple radially assembled Ib oligomers (referred to as Ib-rosette) **(Extended Data Fig. 1a, b)**. Focusing on the units of the oligomers, single particle structural analysis using CryoSPARC[27] revealed that Ib-rosette contained not only particles of Ib-pores with membrane−spanning regions covered by lipid micelles, but also particles of Ib-prepores where the β-barrel was not yet formed (**Extended Data Fig. 1c–g**). The prepore particle data set could be further classified into five subclasses: particles with an open central (class 1) region and particles with a constricted central structure where the base of the β-barrel has formed but is still immature (class 5) **(Extended Data Fig. 2a)**. Class 2–4 suggested that the particle data set was composed of protomers in multiple states, because the density of some portion in the protomers were averaged out. Detailed structural analysis at the protomer level with symmetry expansion **(Extended Data Fig. 2b)**, focused 3D classification **(Extended Data Fig. 2c–d)**, refinement using appropriate reference map for each class and further focused 3D classification **(Extended Data Fig. 2e–g)**, revealed that the heptameric prepore state is formed by three distinct protomer states, which differ from those in the pore state: the initial state, early intermediate state (early int.), and late intermediate (late int.). Finally, the particle data sets for prepore class 1–4 were classified into eight classes, reflecting the different proportions of these three states **(Fig. 1a–j, Extended Data Fig. 2h–i).** The structural characteristics of each protomer's state are described in the following sections **(Fig. 2)**.

During the single particle analysis of the Ib-pore, multiple pore states with varying degrees of β-barrel maturation were observed. These states exhibit no distinguishing features other than the length of the β-barrel. Focusing on the particle set that formed a fully extended β-barrel, particle images were selected for density map calculation **(Fig. 1k)**. Atomic models were refined against the density maps of the prepores and the pore, allowing for a comparative analysis of their structural characteristics.

Structure comparison of Ib protomers

Ib consists of four domains: D1, which binds to the enzymatic component Ia; D2, which forms the pore lumen; D3, which interacts with other domains within a protomer and contributes to structural stabilisation directly; and D4, which is responsible for binding to the target cell receptor **(Fig. 2a–c)**. D2 can be further subdivided into D2c which serves as the structural foundation of the oligomer, and D2s which form β-barrel upon pore formation. Structural changes were observed in both of D2c and D2s. The constriction which was found in classification of Prepores **(Extended Data Fig. 2a),** corresponds to the conformational change of D2c toward centre of the oligomer. Based on the density of D2s, the protomer's state could be roughly distinguished into two state as D2s visible protomer and D2s invisible protomer, which contributed as a key indicator to classify multiple prepore classes during the single particle analysis **(Extended Data Fig. 2c)**. In addition, atomic model building against the density map of D2c revealed that D2s visible protomer could be further subdivided into two classes due to the slight conformational difference, which we termed as Initial state **(Fig. 2d, g**) and Early int. **(Fig. 2e, h**), respectively. We also termed the D2s invisible protomer as Late int. **(Fig. 2f, i).** Consequently, the prepores comprised protomers in three distinct states, except for the pore state **(Fig. 2d–i, Supplementary Movie 1)**. Including the pore state, the most significant structural differences were observed for D2c and D2s **(Fig. 2j),** and no changes were observed in the Ca-edge and NSQ-loop which are the binding sites for enzymatic component Ia in each structure.

Among three protomer's state, initial state was termed as it because the structure was the most similar to monomeric structural state of CDTb (PDBID:8DCM) and PA (PDBID:1ACC) reported in previous studies **(Extended Data Fig. 4)**[28,29]. On the other hand, both Early int. and Late int. had structural difference from initial state, which were partially similar to the Pore state. Compared to the initial state, the Early int. had a structure where β7 and β8 on the D2c domain at the protomer interface were shifted towards the CCW (counter-clockwise) **(Fig. 2k, Supplementary Movie 2)**, when top is defined as enzymatic component binding site and CCW is relative this orientation. In addition to the difference in D2s visibility, in the Late int., the position of α5 on the D2c domain was observed to shift towards the centre of the oligomer **(Fig. 2l)** comparing to the Early int. The Late int. was quite similar to the structure of the pore (Pore state), except that the β-barrel has not yet formed, and there was difference in the position of α5. A structural comparison of the Late int. and the Pore state is described in the following section. Based on these structural difference in D2s and D2c, the series of structures was suggested to change in the order of Initial state, Early int., Late int., and Pore state **(Supplementary Movie 1)**. The increase of backbone root mean square deviation (RMSD)

value for Initial state compared to Early int. (0.568 Å), Late int. (0.789 Å), and Pore state (0.822 Å), supported this structural transition manner. Furthermore, the RMSD values for Late int. compared to Ealry int. (0.721 Å) and to Pore state (0.656 Å) suggested that Late int. has greater similarity with Pore state than Early int.

The arrangements of the three types of protomers that constituted the prepores obtained in this analysis were distinctive. From Prepore I to VIII, the number of protomers in the Initial state decreased by one, whereas the number of protomers in the Late int. increased by one. In addition, Late int. protomers were not scattered throughout the oligomer but were adjacent to each other **(Fig. 1a–h, Extended Data Fig. 5)**. These structural features suggested that the maturation of Pore completes through step-by-step conformational change from Prepore I to Prepore VIII in a domino-like manner, temporarily losing its symmetry. Another notable feature is that there was always one Early int. in the CW direction from a Late int.

Conformational change at the protomers interface

It was necessary to consider what influences the adjacent protomer's structure, which induces the conformational changes. Therefore, structural comparisons were made in pairs of protomers. In the Initial state-Initial state interface, the structure around β7-8 showed a gap **(Fig. 3a, b)**. In contrast, at the Early int.-Late int. interface, the structure was tightly zipped **(Fig. 3c, d)** by the shift of β7 and β8 which is observed in transition from Initial state to Early int. **(Fig. 2k)**, increasing the varied surface area of the interface **(Supplementary Movie 2)**. In other words, the initial structural change between the protomers is a process of reducing the solvent-exposed surface area and gaining interactions between the protomer pairs.

Next, the structural difference in the Early int.-Late int. interface and Late int.-Late int. interface were examined. However, no significant structural changes were observed at these interfaces. Prepore VIII formed by seven Late int. protomers, was found to have a relatively constricted structure with a more densely filled central density than earlier prepores **(Fig. 3e–h, Extended Data Fig. 6)**. This density could be explained as the residues forming the constriction-site known as the ϕ-clamp. Since the residues forming the ϕ-clamp (aa. 451–458) are located near α5 (aa. 460–473), it is reasonable that the shift of α5 toward the centre of oligomer observed from Early int. to Late int. led the formation of the ϕ-clamp **(Fig. 2l, Supplementary Movie 1, 3)**. The increase of protomers in Late int. through Prepore I to Prepore VIII allows gradual formation of ϕ-clamp, which facilitate protomers in Late int. to be adjacent each other resulting in domino-like manner and step-by-step transition to Prepore VIII. Although the ϕ-clamp

230 forming residues in Late int. in Prepore II–VIII shift toward the centre of oligomer to form ϕ-
231 clamp as well as Prepore VIII, the corresponding density was not observed in these maps,
232 suggesting the structure is flexible. In Prepore VIII, although the density around the ϕ-clamp
233 allowed for tracing the main chain structure, the side chains were not clearly observed even at
234 the high resolution.
235
236 **High-resolution structure of Ib-pore**
237 In our previous study, we determined the structures of Ib-pores solubilized with LMNG and the
238 Ia-bound Ib-pore complex. The map of Ib-pore without Ia was obtained only in an immature
239 short β-barrel state, while the map of Ia-bound Ib-pore was obtained in both short β-barrel and
240 fully formed β-barrel states. Due to the Ia bound on to the Ib-pore, applying C7 symmetry
241 during map calculation for the fully formed β-barrel was not feasible, which limited the
242 resolution. In this study, we successfully obtained a high-resolution map of the Ib-pore with a
243 fully formed β-barrel, allowing clear density observation up to the tip of the β-barrel, compared
244 with previous research **(Fig. 4a, b)**. The Ib-pore contains several distinct constriction-sites
245 within its lumen **(Fig. 4c)**. As described in the previous section, the Ca-edge and the NSQ-loop
246 which are involved in binding to the enzymatic component, did not undergo structural changes
247 from the prepore to the pore **(Fig. 2c)**. The most significantly changed constriction-site was the
248 ϕ-clamp which was not observed in Prepore I, showed relatively unclear density in Prepore VIII
249 **(Fig. 3g, h)**, and was clearly observed in Ib-pore **(Fig. 4d, Extended Data Fig. 6)**.
250
251 In the density obtained at the tip of the β-barrel, the hydroxyl groups of Y356 and Y344 were
252 oriented outwards from the TM region, showing the characteristic snorkelling effect of
253 transmembrane proteins. The amino acid side chains oriented inward in the β-barrel are rich in
254 Ser/Thr and are relatively small. The side chain density of Q345, located at the hairpin turn of
255 the β-barrel extended towards the centre, indicating a constriction **(Fig. 4c, e)**. However, the
256 side chain density was relatively unclear and the side chains were far from each other, which
257 suggested that the structure was flexible. Furthermore, in the Pore state, α5 was shown to shift
258 towards the base of the β-barrel from Prepore VIII, forming interactions and stabilising the
259 structure **(Fig. 4f, g, Supplementary Movie 3)**.
260
261
262
263

Discussion

In this study, cryo-EM analysis of Ib-rosette which is the super-complex of a bacterial PFT revealed the step-by-step conformational changes as they transitioned from soluble prepore to membrane-spanning pore. Although the general mode of action of PFTs is widely recognised, detailed insights into their structural changes have mostly been based on comparisons of a few stable states and biochemical experiments with mutants. Being supported by cryo-EM density maps, we uncovered multiple structures including intermediate states during pore formation **(Fig. 1)**: the early immature state of soluble monomers forming a symmetric oligomer (Prepore I), asymmetric oligomers with structural changes in some protomers (Prepore II-VII), the fully matured symmetric Prepore VIII, and Pore with the membrane translocating the β-barrel. This is the first report for PFP family to reveal multiple intermediate structures in the membrane pore maturation process, supported by cryo-EM density maps without false symmetry by strategic analysis workflow **(Extended Data Fig. 2)**. These structural comparisons improve our understanding of conformational changes within individual protomers and allow for a more thorough discussion of the overall maturation process of binary toxin pores.

In our previous cryo-EM study of the Iota toxin, we determined the structures of both the Ib-pore and the Ia-bound Ib-pore complex (as well as the CDTa-bound CDTb-pore complex), revealing the docking mode of the enzymatic component as the initial step of its translocation through the Ib-pore, and showed that the N-terminus undergoes unfolding, which allows pass through ϕ-clamp which is the narrowest constriction-site of Ib-pore[20,21]. The results of this study revealed the detailed structures of the earlier steps, facilitated a more comprehensive understanding of the cellular entry mechanisms of binary toxins. Scott et al. also reported that the structural variety among PA protomers within the oligomer was classified into distinct states, using cryo-EM analysis of the D425A mutant of the anthrax toxin PA (which inhibits pore formation) based on the appearance of the density map of the receptor-binding domain. Moreover, protomers with similar structural states tend to be adjacent to each other within oligomer[26]. Expanding upon the previous report, we classified various protomer states based on their structural features on D2c and D2s using cryo-EM analysis and wild-type *Clostridium perfringens* iota toxin Ib samples. We identified the characteristic structural changes in the protomers and classified them into four states: Initial state, Early int., Late int., and Pore state. In addition, multiple structure of the entire oligomer differing in the ratio of each protomer's state, were successfully identified. Furthermore, these protomer states were distributed in a distinctive pattern, in which the Late int. are always adjacent to each other at Early int. and was positioned in the most CCW direction within the oligomer, suggesting a regularity in the structural transition process **(Fig. 1a–h)**.

Initially, we aimed to prepare the Ib-pores in a lipid membrane environment using liposomes for solubilisation. However, the particles obtained were not proteoliposomes but rather aggregates of Ib oligomers assembled radially **(Extended Data Fig. 1a)**. Similar aggregates have been observed in the oligomers of the anthrax toxin PA, another binary toxin. It has been reported that such structures can be obtained by incubating oligomers bound to a carrier under acidic conditions[30]. However, unlike this study, structural analysis of the constituent oligomers has not been achieved. The antigen component of the influenza virus vaccine forms a radial structure composed of HA proteins referred to as the HA rosette[31,32]. Following this convention, we refer to the aggregated Ib structure as the Ib-rosette.

The Ib-rosette is an aggregate composed of multiple Ib oligomers; however, single particle structural analysis was possible by focusing on each oligomer. During the analysis, it was found that these oligomers included structures without β-barrels, partially formed β-barrels, and fully formed β-barrel **(Extended Data Fig. 1c–g)**. When observing the two-dimensional average images of the prepore class, an ambiguous density was found in the side view in the direction where the β-barrel would form **(Extended Data Fig. 1f, g)**. This indicated that other oligomers in Ib-rosette spatially hinder the formation of the β-barrel. In CDTb, it is known that paired heptamers form a dimer of heptamers; however, clear two-dimensional images of each heptamer are observed in these cases. In case of Ib-rosette sample, the average images of this prepore classes were clearly different[33,34]. We performed a more detailed classification of the prepore classes and obtained density maps for each of the eight prepores and the pore **(Fig. 1, Extended Data Fig. 2)**.

The multiple density maps obtained by Cryo-EM are independent of each other, making it difficult to interpret their correspondences. For example, in this study, it is not possible to establish a direct correspondence of protomers across different prepore states. Specifically, it remains uncertain whether the Early int. protomer observed in Prepore II undergoes a structural transition to the Late int. in Prepore III that is referred as CW model **(Fig. 5e–g)**, or retains its structure as an Early int. without any transition that is referred as CCW model **(Fig. 5h–j)**. At least, observations from a series of prepore maps suggest that the Ib-prepore adopts conformational changes through asymmetric intermediate structural states in step-by-step and domino-like manner. Based on these findings, we propose a possible structural transition models of the pore maturation in this study **(Fig. 5)**.

335 Comparison of the series of cryo-EM maps demonstrated formation of ϕ-clamp at the
336 centre of the oligomer along with the pore maturation **(Extended Data Fig. 6)**. Phenylalanine
337 residue forming ϕ-clamp is highly conserved among binary toxin family, and mutational study
338 using anthrax toxin PA have revealed its critical role in maturation from the prepore to the
339 pore[24]. The F454 residue of Ib is located upstream of α5 (aa. 460–473), which undergoes the
340 most significant structural shift during the transition from Early int. to Late int. The density of
341 the residues surrounding F454 (aa. 449–460) was not observed in the Initial state or Early int.,
342 suggesting that these residues possess a flexible structure in the states **(Fig. 3f)**. In the Late int.,
343 the density became more apparent especially in Prepore VIII, where the main-chain structure
344 could be roughly traced. This observation indicates that the constricted region could be formed
345 between a pair of protomers in Late int **(Fig. 3h)**. Because no significant structural changes
346 were observed in the contact interface between the Late int.-Late int. pair and the pair that could
347 be considered its precursor, we could not identify the factors contributing to the proximity of
348 Late states. Although the most notable change in the Late int. is the movement of α5, this
349 movement occurs away from the adjacent protomer, making it unlikely to stabilize the adjacent
350 protomer into Late int. On the other hand, residues around the ϕ-clamp which show significant
351 changes, are positioned to interact with each other. Therefore, the partial formation of the ϕ-
352 clamp which is associated with the movement of α5, might facilitate to the tendency of Late int.
353 states to come into proximity. Notably, despite of the high-resolution map of Prepore VIII at 2.9 Å,
354 the side chains of residues forming ϕ-clamp was not observed, indicating the structural flexibility.
355 Even at the similar resolution at 2.9 Å, the density is clearly observed in previously reported Ib-
356 pore map (EMD-0721). Considering further structural shift of α5 during the transition from
357 prepore VIII to pore as well **(Supplementary Movie 3)**, additional stabilization could be
358 occurred, resulting in formation of stable ϕ-clamp in pore **(Fig. 5j, k)**.
359
360
361 The enzymatic components believed to pass through the pores exhibit different
362 stoichiometries and binding positions in the iota toxin and anthrax toxins. In anthrax toxin, three
363 enzyme molecules LF and EF bind to a single pore, with their N-terminal α-helices interacting
364 with the α-clamp formed at the interface of PA protomers[35–37], which makes the N-terminal α-
365 helices face forwards to ϕ-clamp. In contrast, the single enzymatic components of the iota toxin
366 and CDT bind to the Ca-edge of the pore, with its N-terminal helix unfolding at the NSQ-
367 loop[20,21]. For binary toxin pores with a narrow constriction such as ϕ-clamp, the docking and
368 unfolding of the enzymatic component from the Ca-edge to the NSQ-loop represent critical
369 steps for activity. Notably, these regions remain unchanged in the structures of the individual
370 monomer's states **(Fig. 2j)**. This suggests that the enzymatic component could bind to the

371 oligomer in both immature prepore state and mature pore states in same docking mode. In
372 addition, the high-resolution cryo-EM density of the pore structure reported in this study
373 revealed a constriction formed by Q345 at the tip of the β-barrel, which served as the exit for
374 membrane translocation **(Fig. 4c, e)**. The diameter of this constriction site is less than 10 Å,
375 which is smaller than the general diameter of an α-helix. Although a clear density was observed
376 in the ϕ-clamp, the density of this constriction was ambiguous, suggesting that its structure is
377 relatively flexible.
378

379 This study has enabled the discussion of the maturation process from Prepore to Pore
380 in binary toxins at the molecular structural level, supported by the cryo-EM density **(Fig. 5)**.
381 However, it should be noted that the observation of these structural states may have been made
382 possible by the formation of the Ib-rosette, which potentially sterically hindered pore formation.
383 Therefore, it is necessary to consider the possibility that the obtained structures may be
384 artefacts, similar to samples in which pore maturation was cancelled by introducing mutations.
385 However, the formation of the Ib-rosette may have enabled the trapping of unstable
386 intermediates that also occurred during the normal transition from the prepore to the pore. Based
387 on a comparison of the obtained structures, we proposed models of pore maturation with step-
388 by-step process. Jiao *et al.* concluded that perforin undergoes a CW structural change by
389 comparing temporal observations of the same molecule using atomic force microscopy (AFM)
390 and specific directional structural perturbations through MD simulations[38]. During the
391 maturation of the prepore, the number of Late ints. protomers increased sequentially. However,
392 due to difficulty in identifying the correspondence of protomers in cryo-EM maps, whether this
393 structural change proceeds via Early int. or directly from the Initial state, corresponding to the
394 CW and CCW models respectively, remains to be investigated. In addition, the domino-like
395 structural change in the prepore progressed through forming a pair of Early int. and Late int. as
396 observed during the transition from Prepore I to Prepore II. However, it is also possible that the
397 maturation process proceeds from more than two initiation points or occurs before heptamer
398 formation. This hypothesis needs to be discussed, considering the speed of the maturation
399 process and the likelihood of the emergence of additional initiation points. Future experiments
400 involving single-molecule observations or simulations are expected to address these challenges
401 and elucidate the detailed mechanisms of pore maturation.

402

403 PFPs are major components of bacterial toxins and the immune system and have
404 become intriguing targets in both fundamental research and applications, such as their use as
405 nanodevices in nanopore sequencing. However, these complicated proteins are produced as

soluble monomers that mature into functional pores through dynamic structural changes. Binary toxins possess unique characteristics among pore-forming toxins that enable the translocation of enzymatic components into target cells via pores, making them highly applicable. Research is being conducted to create carriers by conjugating proteins to the binding domain of the enzymatic component, facilitating the intracellular delivery of the desired molecules[24,39]. This study is the first report of multiple structural states during the pore-forming process of a binary toxin through detailed classification using cryo-EM, which was previously difficult to obtain. Furthermore, we also expect that the findings of this study will facilitate our understanding of the general maturation processes of PFPs in general and contribute to the advancement of nanodevice development based on this structural foundation.

418 **Methods**

419 **Expression and purification of Ib**

420 Ib was expressed with a 20 kDa pro-sequence at the N-terminus which inhibits
421 oligomer formation, and a 6-His tag at the C-terminus. Specifically, the gene encoding Ib
422 (Uniprot ID: Q46221, residues 40–875) was cloned into pET23a without the signal sequence or
423 other tags. The plasmid was transformed into *Escherichia coli* BL21 (DE3) and cultured in LB
424 medium containing 50 ng/μl ampicillin at 37°C. When the culture reached an OD600 of 0.6,
425 IPTG was added to a final concentration of 1 mM, and the culture was incubated for an
426 additional 16 hours at 23°C. The cells were harvested by centrifugation.
427

428 The harvested cells were resuspended in buffer A (20 mM Tris pH 8.0, 100 mM NaCl, 1.0 mM
429 CaCl2, 20 mM imidazole) containing one complete ULTRA Tablet (Roche, Basel, Switzerland)
430 and lysed by sonication on ice. The lysate was subjected to ultracentrifugation (180,000*g*, 40
431 min) and the soluble fraction was bound to a Ni-NTA column. The column was washed with 10
432 volumes of buffer A and eluted with buffer B (20 mM Tris, pH 8.0, 100 mM NaCl, 1.0 mM
433 CaCl2, and 500 mM imidazole). The eluate was concentrated by centrifugation using a 50 K
434 ultrafiltration membrane and exchanged with buffer C (20 mM Tris, pH 8.0, 100 mM NaCl, 1.0
435 mM CaCl2).

436

437 **Sample preparation of Ib-rosette**

438 Ib was activated and oligomerised in our previous studies[6]. Monomeric Ib was
439 incubated at room temperature for 1 h with chymotrypsin at a 1/1,000 mass ratio. The reaction
440 was stopped by adding PMSF (phenylmethylsulfonyl fluoride) at a final concentration of 1 mM
441 to inhibit chymotrypsin activity. Ethanol was then added to a final concentration of 10% (v/v),
442 and the mixture was incubated at 37°C for 1 h to promote Ib oligomerisation. 450 μl of the Ib
443 oligomer solution was added to a Ni-NTA resin and washed with buffer C to remove ethanol.
444 540 μl of prepared liposomes (made by drying E. coli Extract Polar (Sigma-Aldrich) under N2
445 gas, resuspending with Buffer C, and processing through an extruder (Sigma-Aldrich) with a
446 100 nm filter), 360 μl of buffer C, and 100 μl of 1 M MES (pH 5.5) were then added, followed
447 by incubation at 4°C for 16 hours. The resin was washed with ten column volumes of buffer A
448 and eluted with buffer B. The eluted product was subjected to gel filtration using HiLoadTM
449 16/200 SuperdexTM 200pg of buffer C at a flow rate of 0.8 mg/ml. Fractions containing the Ib
450 oligomer bands were collected based on SDS-PAGE observation and concentrated to 1.0 mg/ml
451 using a 50 K ultrafiltration membrane.
452

453 **Data collection with Cryo-EM**

454 The prepared sample (3 µl) was applied to hydrophilised Quantifoil R1.2/1.3, 300
455 mesh (Cu), and blotted for 7 seconds using a Vitrobot Mark IV (Thermo Fisher Scientific),
456 followed by rapid freezing in liquid ethane. The frozen grids were imaged using Glacios
457 (Thermo Fisher Scientific) equipped with a Falcon4 direct electron detector at the Institute for
458 Life and Medical Sciences at Kyoto University to screen the grid preparation conditions through
459 single-particle analysis. The final data were collected using a Titan Krios (Thermo Fisher
460 Scientific) equipped with a K3 direct electron detector (Gatan), a BioQuantum energy filter
461 (Gatan) with a slit width of 20 eV, and a Cs corrector (CEOS, GmbH) at the Institute for Protein
462 Research, Osaka University, with a pixel size of 0.88 Å/pix, capturing 11,549 micrographs. The
463 detailed imaging conditions are listed in Table 1.

464

465 **Single particle analysis of Ib-pore**

466 A series of analyses of the cryo-EM images was conducted using CryoSPARC
467 (ver.3.3.2.)[27]. Motion correction was performed using Patch Motion Correction, and CTF
468 estimation was performed using Patch CTF Estimation. Particle images were obtained using a
469 Template Picker with a reference created by back-projecting a previously reported Ib-pore
470 density map (EMD-0721). The particle images were extracted and downscaled to 1/4 of their
471 original size. These extracted particles were roughly classified through Heterogeneous
472 Refinement with C7 symmetry applied, resulting in a distinction between the prepore class,
473 which lacks a β-barrel, and the pore class which has a β-barrel. The detailed analysis of the
474 prepore class is described later in the "Classification of Ib-prepore" section. More homologous
475 particle images were selected for the pore class through 3D Variability Analysis (3DVA)[40] and
476 no-align 3D classification. The resulting particle set was re-extracted without rescaling, and a
477 3D density map was reconstructed using Homogeneous Refinement. Additionally, Local
478 Motion Correction[41] was performed to correct for per-particle motion, followed by
479 Homogeneous Refinement of images with defocus correction[42]. The local resolution was
480 estimated with the RELION[43] Local Resolution job **(Extended Data Fig. 3)**.

481

482 **Classification of Ib-prepore**

483 3DVA was performed on the prepore class, resulting in the classification of circular
484 oligomers into five distinct subclasses ranging from an expanded state to a more constricted
485 state **(Extended Data Fig. 2a)**. Class 5 which is the most constricted class, exhibited a structure
486 partially forming a β-barrel, similar to the Pore state; thus, further analysis was not conducted
487 for this class. The remaining classes 1–4 were subjected to Symmetry Expansion with C7
488 symmetry, where the particle images were symmetrically replicated seven times. A mask was

created focusing on one protomer, and the 3DVA of the protomer was used to distinguish between classes with and without an observable density corresponding to the D2s within the protomer (**Extended Data Fig. 2b, c**). For Classes 1 and 2, the maps were reconstructed using Homogeneous Reconstruction Only with the particle sets where D2s were not visible, whereas Classes 3 and 4 used particle sets where D2s were visible. These reconstructions were references for refining the original particle sets before replication using Nonuniform Refinement. Among the resulting density maps, protomers where D2s were ambiguously visible, were subjected to focused non-aligned 3D classification to separate classes where D2s were visible from those where they were not; this process was iteratively repeated (**Extended Data Fig. 2e–g**). Ultimately, the prepore states were classified into eight distinct classes, each differing in the number of protomers with clearly visible D2s. Finally, Non-uniform Refinement[44] and Local refinement were performed for each of the eight prepore classes. The local resolution was estimated with the RELION[43] Local Resolution job (**Extended Data Fig. 3**).

Model building

As structures such as the initial state and early int. where D2s are folded within the protomer, have not been previously reported in Ib, the predicted models were used as the initial model. The structure predicted from the Alphafold Database was edited to start the residue numbering from 1 after the signal sequence based on the amino acid sequence of Ib (Uniplot ID: Q46221), and used as the initial atomic model for the initial state. The predicted model was fitted as a rigid body into the most clearly observed initial state density in the Prepore I map using UCSF ChimeraX (ver.1.2.4)[45], followed by manual model refinement using Coot (ver.0.9.5)[46] and automated structural refinement using PHENIX (ver.1.19.2)[47]. For Early int., the refined initial state was used as the starting model. In contrast, for late int. and the pore state, the known Ib-pore structure (PDBID:6KLW) was used as the starting model and refinement was conducted against the respective density maps of Prepore II–VIII, and Pore in the same manner as described above. Although the D4-I structure of Ib has not been previously reported, its density was observed in Prepore I. Therefore, the refined D4-I structure from Prepore I was used as the initial model for other oligomers and structural refinement was conducted again using PHENIX. Finally, the chain orientations were validated using MolProbity[48] for the models obtained using the above process. Inner radius of Ib-pore was calculated using HOLE2[49] software.

Data availability statement

The Cryo-EM maps and coordinates were deposited to the Electron Microscopy Data Bank (EMDB) and Protein Data Bank (PDB) with the accession codes EMD-61772 and PDBID 9JSG for Pore state, EMD-61771 and PDBID 9JSF for Prepore I, EMD-61774 and PDBID 9JSI for Prepore VII, EMD-61773 and PDBID 9JSH for Prepore III, EMD-61775 and PDBID 9JSK for Prepore IV, EMD-61776 and PDBID 9JSL for Prepore V, EMD-61777 and PDBID 9JSM for Prepore VI, EMD-61778 and PDBID 9JSN for Prepore VII, and EMD-61779 and PDBID 9JSO for Prepore VIII. The cryo-EM images are deposited to Electron Microscopy Public Image Analysis (EMPIAR) with the accession code EMPIAR-12333.

Acknowledgements

This work was supported by JSPS KAKENHI Grant Numbers 21H02452 (to H.T.), 24K01993 (to H.T.), and 21J13410 (to T.Y). This research was partially supported by the Platform Project for Supporting Drug Discovery and Life Science Research (Basis for Supporting Innovative Drug Discovery and Life Science Research (BINDS)) from AMED under Grant Number 2366 and the Joint Usage/Research Center Program of the Institute for Life and Medical Sciences at Kyoto University (to H.Y., Y.S., and T.N.). We thank J. Kishikawa, M. Hirose, and T. Kato at the Institution for Protein Research, Osaka University, for training on the techniques used for the cryo-EM study. We would like to thank Editage (www.editage.jp) for English language editing

Author contribution

All author participated in research design; T.Yamada prepared the Ib-rosette sample for cryo-EM; T.Yamada, Y.S and T.N performed cryo-EM data collection, and T.Yamada and Y.S performed single particle analysis; T.Yamada and T.Yoshida performed the atomic model building; all authors contributed to the discussion and writing the manuscript, and H.T supervised the project.

Author information

Competing interests: The authors declare no competing interests.

553 **Figure and figure legends**

554

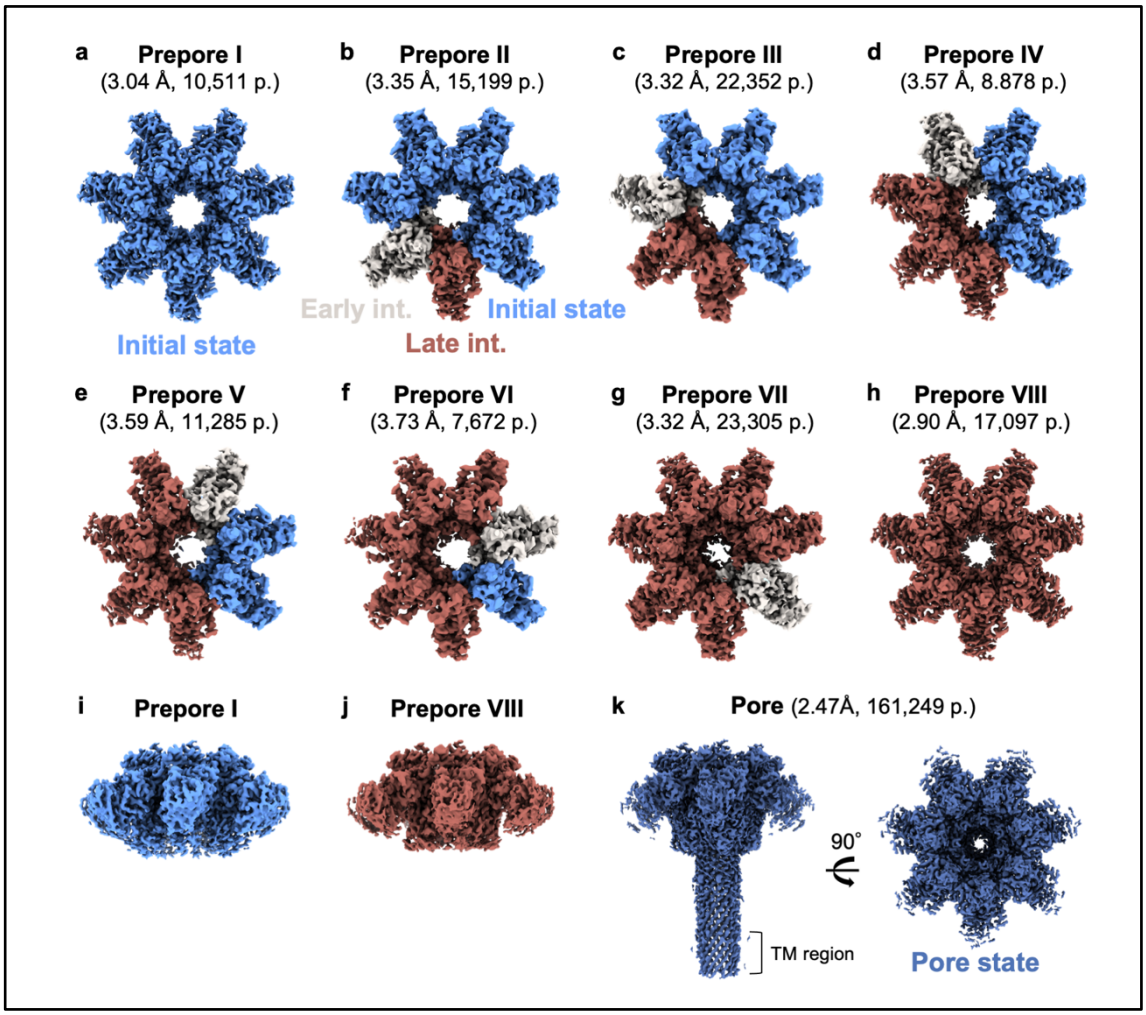

555

556 **Figure 1 | Cryo-EM maps obtained from Ib-rosette analysis**

557 **a–j** Cryo-EM maps of Ib-prepores obtained from cryo-EM single-particle analysis. **a–h** are
558 views from the top of the prepore where the enzymatic component Ia docks. **i, j** Side views of
559 Prepore I and Prepore VIII indicate that the membrane-spanning-barrel has not yet formed at
560 these stages. **k** Cryo-EM map of Ib-pore viewed from the side (left) and top (right).

561

562

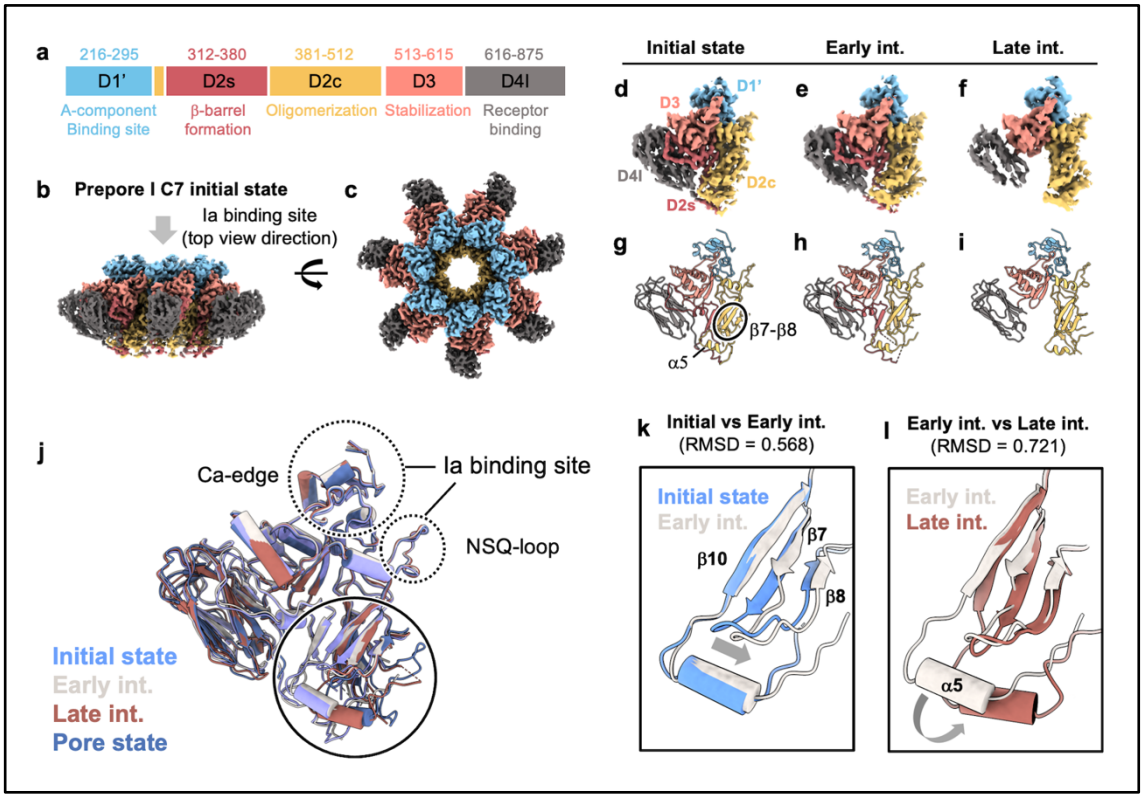

Figure 2 | Structures of Ib protomer

a Schematic of the N-terminal cleaved Ib domains with densities observed in cryo-EM maps. **b, c** Cryo-EM maps of Prepore I, coloured according to the domains shown in panel **a**. **d–i** Maps and atomic models of the Ib protomer, coloured according to the domains. The Initial state map was extracted from the Prepore I, Early int. from Prepore II, and the Late int. in Prepore VIII. **j** Atomic models of the Initial state from Prepore I, Early int. from Prepore II, Late int. from Prepore VIII, and Pore state from Pore were aligned. **k, l** Comparison of cartoon models with tube α-helix between the Initial state (cyan) vs. Early int. (white), and Early int. vs. Late int. (brown). The RMSD values were calculated using UCSF Chimerax[45].

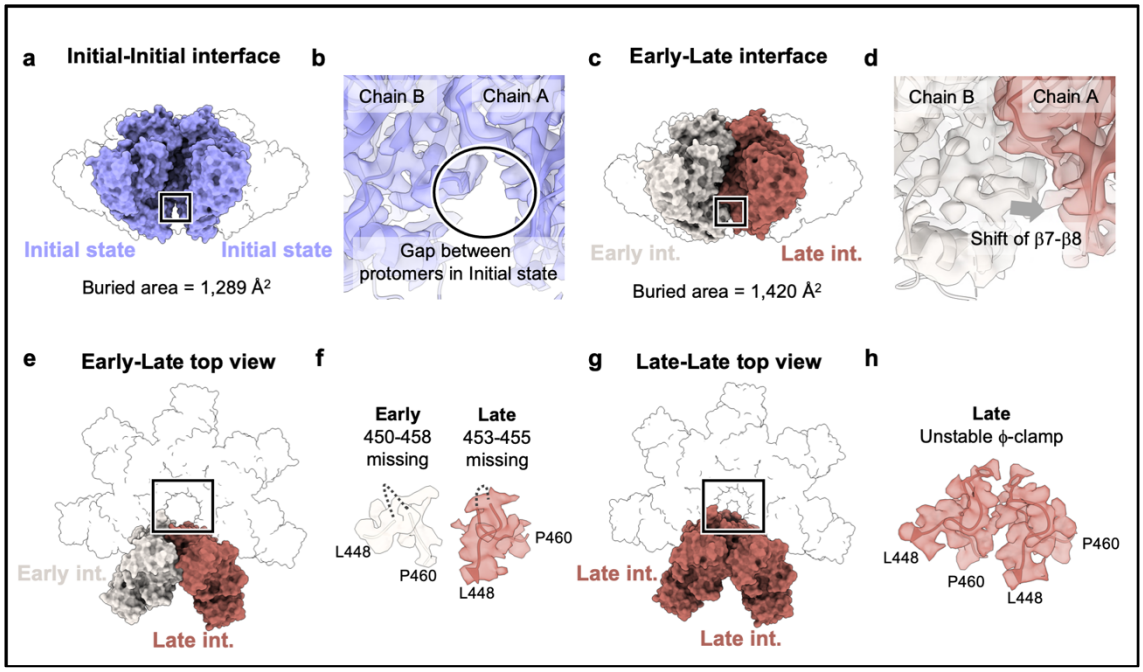

Figure 3 | Comparison of inter-protomer interactions

a–d Comparison of interface structures between the Initial state and the Initial state (Prepore I) and the interface structure between the Early int. and Late int. (Prepore II). **a, c** Surface models of interest calculated from atomic models of Prepore I and Prepore II. **b, d** Atomic models in respective cryo-EM density maps. **e–h** Comparison of constriction-site structures between the Early int. and Late int. (Prepore II) and the interface structure between the Late int. state and Late int. (Prepore VIII). **e, g** Surface models of interest calculated from the atomic models of Prepores II and VIII. **f, h** Diagram of the atomic model in the ϕ-clamp map, generated with residues 448–460, and the density map trimmed around the atoms.

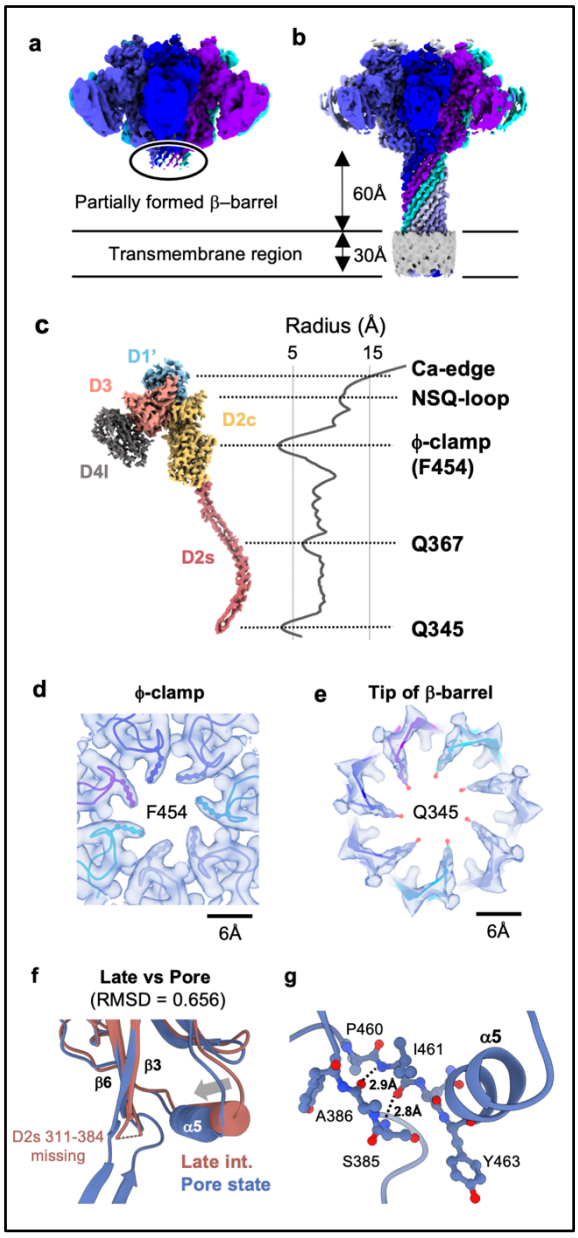

Figure 4 | Structure of Ib-pore

a, b Cryo-EM maps of Ib-pores with immature-barrel (see Extended Data Fig.2a) and fully formed-barrel. The maps are coloured according to the protomers. **c** Cryo-EM map of an Ib protomer extracted from the Ib-pore with a fully formed barrel. The inner radius was calculated using HOLE2[49] software. The positions of the constriction sites in the Ib-pore are marked with dotted lines. **d, e** Diagrams of the model showing the smallest inner radius. **f** Comparison of cartoons between Late int (brown) and the Pore state (purple). **g** Atomic model of Pore state Ib.

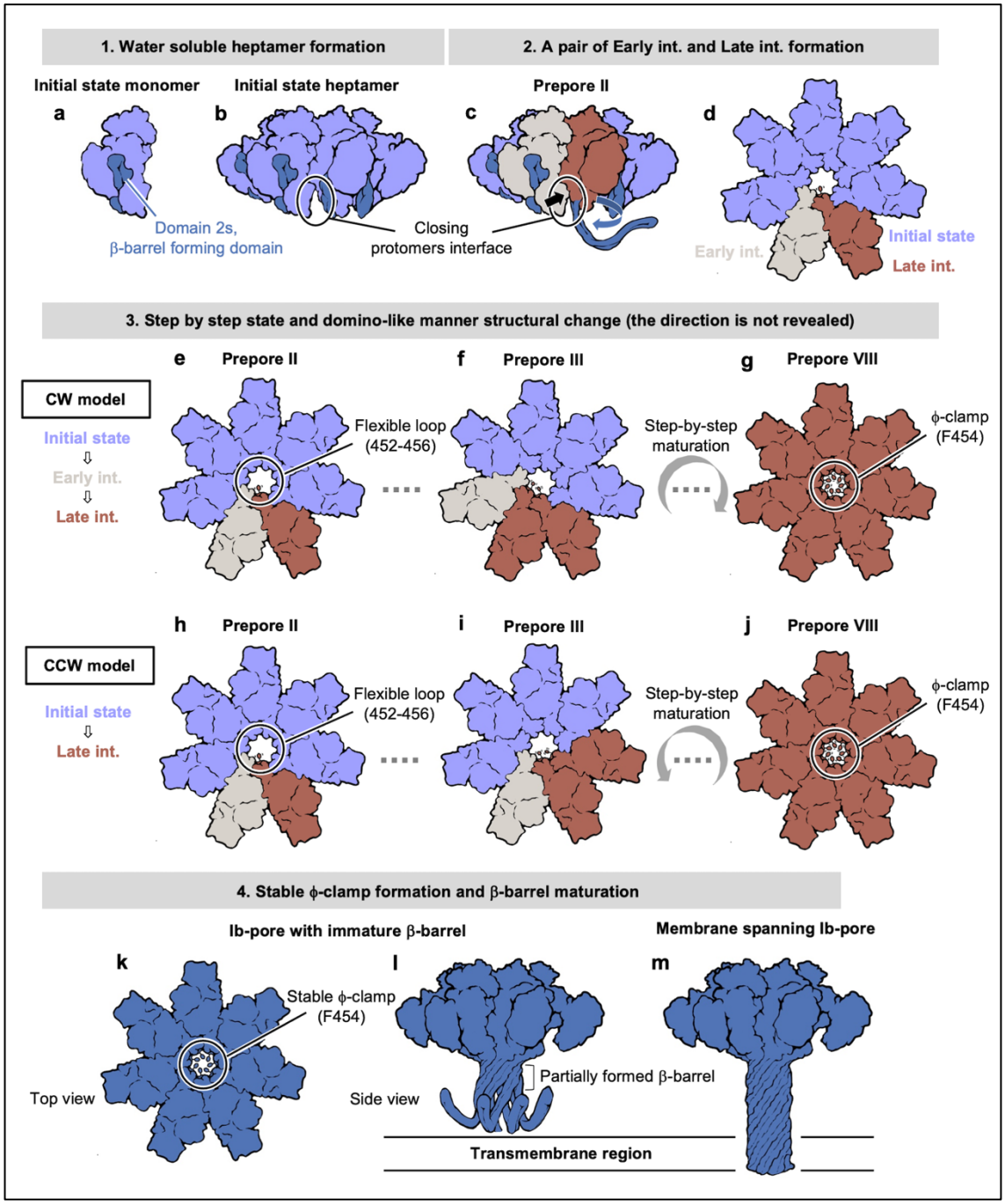

Figure 5 | Summary of Ib-pore maturation mechanism

a N-terminal cleaved active Ib monomer in its Initial state. **b** Active Ib monomers assemble into heptameric Prepore I. **c** Two adjacent protomers convert into a pair of Early int. (white), and Late int. (Red) (Prepore II). **d** Top view of Prepore II. **e–g, h–j** Top views of the respective Ib-prepores. Number of Initial states and Late int. changed with step-by-step domino-like manner propagation in either CW or CCW direction. **g, j** The central constriction-site of the Ib-prepore is not yet fully formed but remains flexible. **k–m** Structures of the Ib-pores **k** Upon maturation

612 to the pore, a stable ϕ-clamp is formed at the central constriction-site. The extension of the long
613 β-barrel was achieved through the partial formation of the β-barrel from the foundation of the
614 oligomer.
615

EMDB ID	Pore EMD-61772	Prepore I EMD-61771	Prepore II EMD-61774	Prepore III EMD-61773	Prepore IV EMD-61775	Prepore V EMD-61776	Prepore VI EMD-61777	Prepore VII EMD-61778	Prepore VIII EMD-61779
Magnification	81,000								
Voltage (kV)	300								
Electron Exposure (e⁻/Å²)	50								
Defocus Range (μm)	-0.6–1.6								
Pixel Size (Å)	0.88								
Symmetry Imposed	C7	C7	C1	C1	C1	C1	C1	C1	C7
Initial Particle Images (No.)	6,223,563								
Final Particle Images (No.)	161,249	10,511	15,199	22,352	8,878	11,285	7,676	23,305	17,097
Map Resolution (Å)	2.47	3.04	3.35	3.32	3.57	3.59	3.73	3.32	2.90
FSC Threshold	0.143								

Table1 1 | Cryo-EM data collection statistics

Table 1 | Statistics of cryo-EM data collection and single particle analysis

PDB ID	Pore 9JSG	Prepore I 9JSF	Prepore II 9JSI	Prepore III 9JSH	Prepore IV 9JSK	Prepore V 9JSL	Prepore VI 9JSM	Prepore VII 9JSN	Prepore VIII 9JSO
Refinement									
Model Resolution (Å)	2.6	3.1	3.3	3.6	3.6	3.7	4.0	3.5	3.1
FSC Threshold	0.5								
Model Composition									
Non-hydrogen Atoms	28,539	27,433	26,596	26,198	25,813	25,496	25,209	24,384	24,619
Protein Residues	3,710	3,563	3,453	3,397	3,343	3,299	3,256	3,207	3,171
Ligands	21	21	21	21	21	21	21	21	21
***B* factor**									
Protein ($Å^2$)	57.22	72.39	16.34	10.89	29.98	31.37	22.09	24.80	71.21
Ligand ($Å^2$)	60.40	60.85	10.12	6.43	24.55	24.25	61.32	19.90	52.68
R.M.S.Deviations									
Bond Lengths	0.008	0.014	0.014	0.012	0.010	0.010	0.008	0.011	0.012
Bond Angles	1.096	1.433	1.148	1.245	1.119	1.389	1.319	1.406	1.508
Validation									
MolProbity Score	1.36	1.65	1.69	1.82	1.73	1.64	1.89	1.53	1.1.69
Clash Score	3.69	5.31	6.57	8.33	7.01	4.71	9.21	4.10	5.51
Poor Rotamers (%)	0.80	0.67	0.33	0.80	0.85	1.06	1.25	0.77	1.49
Ramachandran Plot									
Favored (%)	96.73	94.63	95.35	94.68	95.05	94.46	95.34	95.23	96.15
Allowed (%)	3.27	5.37	4.62	5.20	4.74	5.35	4.45	4.65	3.85
Disallowed (%)	0.00	0.00	0.03	0.12	0.21	0.18	0.22	0.13	0.00

Table 2 | Refinement and validation statistics

619

620 **Table 2 | Statistics of atomic model refinement**

621

622

623

Reference

1. Bischofberger, M., Iacovache, I. & van der Goot, F. G. Pathogenic pore-forming proteins: function and host response. *Cell Host Microbe* **12**, 266–275 (2012).
2. Li, Y. *et al.* Structural Basis of the Pore-Forming Toxin/Membrane Interaction. *Toxins* **13**, 128 (2021).
3. Simpson, L. L., Stiles, B. G., Zepeda, H. H. & Wilkins, T. D. Molecular basis for the pathological actions of Clostridium perfringens iota toxin. *Infect. Immun.* **55**, 118–122 (1987).
4. Perelle, S., Gibert, M., Bourlioux, P., Corthier, G. & Popoff, M. R. Production of a complete binary toxin (actin-specific ADP-ribosyltransferase) by Clostridium difficile CD196. *Infect. Immun.* **65**, 1402–1407 (1997).
5. Popoff, M. R. & Boquet, P. Clostridium spiroforme toxin is a binary toxin which ADP-ribosylates cellular actin. *Biochem. Biophys. Res. Commun.* **152**, 1361–1368 (1988).
6. Aktories, K. *et al.* Botulinum C2 toxin ADP-ribosylates actin. *Nature* **322**, 390–392 (1986).
7. Liu, W. & Nestorovich, E. M. Anthrax toxin channel: What we know based on over 30 years of research. *Biochim. Biophys. Acta BBA - Biomembr.* **1863**, 183715 (2021).
8. Knapp, O., Benz, R. & Popoff, M. R. Pore-forming activity of clostridial binary toxins. *Biochim. Biophys. Acta BBA - Biomembr.* **1858**, 512–525 (2016).
9. Nagahama, M. *et al.* Clostridium perfringens Iota-Toxin b Induces Rapid Cell Necrosis ▿ . *Infect. Immun.* **79**, 4353–4360 (2011).
10. Sakurai, J. & Kobayashi, K. Lethal and dermonecrotic activities of Clostridium perfringens lota toxin: biological activities induced by cooperation of two nonlinked components. *Microbiol. Immunol.* **39**, 249–253 (1995).
11. Stiles, B. G. & Wilkins, T. D. Purification and characterization of Clostridium perfringens iota toxin: dependence on two nonlinked proteins for biological activity. *Infect. Immun.* **54**, 683–688 (1986).
12. Gordon, V. M., Leppla, S. H. & Hewlett, E. L. Inhibitors of receptor-mediated endocytosis block the entry of Bacillus anthracis adenylate cyclase toxin but not that of Bordetella pertussis adenylate cyclase toxin. *Infect. Immun.* **56**, 1066–1069 (1988).
13. Barth, H. *et al.* Cellular uptake of Clostridium botulinum C2 toxin requires oligomerization and acidification. *J. Biol. Chem.* **275**, 18704–18711 (2000).

14. Schering, B., Bärmann, M., Chhatwal, G. S., Geipel, U. & Aktories, K. ADP-ribosylation of skeletal muscle and non-muscle actin by Clostridium perfringens iota toxin. *Eur. J. Biochem.* **171**, 225–229 (1988).
15. Reuner, K. H., Presek, P., Boschek, C. B. & Aktories, K. Botulinum C2 toxin ADP-ribosylates actin and disorganizes the microfilament network in intact cells. *Eur. J. Cell Biol.* **43**, 134–140 (1987).
16. Duesbery, N. S. *et al.* Proteolytic Inactivation of MAP-Kinase-Kinase by Anthrax Lethal Factor. *Science* **280**, 734–737 (1998).
17. Leppla, S. H. Anthrax toxin edema factor: a bacterial adenylate cyclase that increases cyclic AMP concentrations of eukaryotic cells. *Proc. Natl. Acad. Sci.* **79**, 3162–3166 (1982).
18. Krantz, B. A. *et al.* A phenylalanine clamp catalyzes protein translocation through the anthrax toxin pore. *Science* **309**, 777–781 (2005).
19. Jiang, J., Pentelute, B. L., Collier, R. J. & Zhou, Z. H. Atomic structure of anthrax protective antigen pore elucidates toxin translocation. *Nature* **521**, 545–549 (2015).
20. Yamada, T. *et al.* Cryo-EM structures reveal translocational unfolding in the clostridial binary iota toxin complex. *Nat. Struct. Mol. Biol.* **27**, 288–296 (2020).
21. Kawamoto, A. *et al.* Cryo-EM structures of the translocational binary toxin complex CDTa-bound CDTb-pore from Clostridioides difficile. *Nat. Commun.* **13**, 6119 (2022).
22. Hardenbrook, N. J. *et al.* Atomic structures of anthrax toxin protective antigen channels bound to partially unfolded lethal and edema factors. *Nat. Commun.* **11**, 840 (2020).
23. Melnyk, R. A. & Collier, R. J. A loop network within the anthrax toxin pore positions the phenylalanine clamp in an active conformation. *Proc. Natl. Acad. Sci. U. S. A.* **103**, 9802–9807 (2006).
24. Sun, J., Lang, A. E., Aktories, K. & Collier, R. J. Phenylalanine-427 of anthrax protective antigen functions in both pore formation and protein translocation. *Proc. Natl. Acad. Sci.* **105**, 4346–4351 (2008).
25. Sellman, B. R., Nassi, S. & Collier, R. J. Point Mutations in Anthrax Protective Antigen That Block Translocation *. *J. Biol. Chem.* **276**, 8371–8376 (2001).
26. Scott, H. *et al.* Structure of the Anthrax Protective Antigen D425A Dominant Negative Mutant Reveals a Stalled Intermediate State of Pore Maturation. *J. Mol. Biol.* **434**, 167548 (2022).

694 27. Punjani, A., Rubinstein, J. L., Fleet, D. J. & Brubaker, M. A. cryoSPARC:
695 algorithms for rapid unsupervised cryo-EM structure determination. *Nat. Methods* **14**,
696 290–296 (2017).
697 28. Goldsmith, J. A., Dewar, V., Hermand, P., Blais, N. & McLellan, J. S.
698 Structural Basis for Binding of Neutralizing Antibodies to Clostridioides difficile
699 Binary Toxin. *J. Bacteriol.* **205**, e00456-22 (2023).
700 29. Petosa, C., Collier, R. J., Klimpel, K. R., Leppla, S. H. & Liddington, R. C.
701 Crystal structure of the anthrax toxin protective antigen. *Nature* **385**, 833–838 (1997).
702 30. Naik, S. *et al.* Monitoring the Kinetics of the pH-Driven Transition of the
703 Anthrax Toxin Prepore to the Pore by Biolayer Interferometry and Surface Plasmon
704 Resonance. *Biochemistry* **52**, 6335–6347 (2013).
705 31. Laver, W. G. & Valentine, R. C. Morphology of the isolated hemagglutinin and
706 neuraminidase subunits of influenza virus. *Virology* **38**, 105–119 (1969).
707 32. Gallagher, J. R. *et al.* Characterization of Hemagglutinin Antigens on Influenza
708 Virus and within Vaccines Using Electron Microscopy. *Vaccines* **6**, 31 (2018).
709 33. Xu, X. *et al.* Structure of the cell-binding component of the Clostridium
710 difficile binary toxin reveals a di-heptamer macromolecular assembly. *Proc. Natl. Acad.*
711 *Sci. U. S. A.* **117**, 1049–1058 (2020).
712 34. Anderson, D. M., Sheedlo, M. J., Jensen, J. L. & Lacy, D. B. Structural
713 Insights into the Transition of Clostridioides difficile Binary Toxin from Prepore to
714 Pore. *Nat. Microbiol.* **5**, 102–107 (2020).
715 35. Feld, G. K. *et al.* Structural basis for the unfolding of anthrax lethal factor by
716 protective antigen oligomers. *Nat. Struct. Mol. Biol.* **17**, 1383–1390 (2010).
717 36. Antoni, C. *et al.* Cryo-EM structure of the fully-loaded asymmetric anthrax
718 lethal toxin in its heptameric pre-pore state. *PLOS Pathog.* **16**, e1008530 (2020).
719 37. Zhou, K. *et al.* Atomic structures of anthrax prechannel bound with full-length
720 lethal and edema factors. *Struct. Lond. Engl. 1993* **28**, 879-887.e3 (2020).
721 38. Jiao, F. *et al.* Perforin-2 clockwise hand-over-hand pre-pore to pore transition
722 mechanism. *Nat. Commun.* **13**, 5039 (2022).
723 39. Rabideau, A. E., Liao, X., Akçay, G. & Pentelute, B. L. Translocation of Non-
724 Canonical Polypeptides into Cells Using Protective Antigen. *Sci. Rep.* **5**, 11944 (2015).
725 40. Punjani, A. & Fleet, D. J. 3D variability analysis: Resolving continuous
726 flexibility and discrete heterogeneity from single particle cryo-EM. *J. Struct. Biol.* **213**,
727 107702 (2021).

41. Rubinstein, J. L. & Brubaker, M. A. Alignment of cryo-EM movies of individual particles by optimization of image translations. *J. Struct. Biol.* **192**, 188–195 (2015).
42. Estimation of high-order aberrations and anisotropic magnification from cryo-EM data sets in RELION-3.1 - PubMed. https://pubmed.ncbi.nlm.nih.gov/32148853/.
43. Scheres, S. H. W. RELION: Implementation of a Bayesian approach to cryo-EM structure determination. *J. Struct. Biol.* **180**, 519–530 (2012).
44. Punjani, A., Zhang, H. & Fleet, D. J. Non-uniform refinement: adaptive regularization improves single-particle cryo-EM reconstruction. *Nat. Methods* **17**, 1214–1221 (2020).
45. Goddard, T. D. *et al.* UCSF ChimeraX: Meeting modern challenges in visualization and analysis. *Protein Sci. Publ. Protein Soc.* **27**, 14–25 (2018).
46. Emsley, P. & Cowtan, K. Coot: model-building tools for molecular graphics. *Acta Crystallogr. D Biol. Crystallogr.* **60**, 2126–2132 (2004).
47. Afonine, P. V. *et al.* Real-space refinement in PHENIX for cryo-EM and crystallography. *Acta Crystallogr. Sect. Struct. Biol.* **74**, 531–544 (2018).
48. Chen, V. B. *et al.* MolProbity: all-atom structure validation for macromolecular crystallography. *Acta Crystallogr. D Biol. Crystallogr.* **66**, 12–21 (2010).
49. Smart, O. S., Neduvelil, J. G., Wang, X., Wallace, B. A. & Sansom, M. S. P. HOLE: A program for the analysis of the pore dimensions of ion channel structural models. *J. Mol. Graph.* **14**, 354–360 (1996).

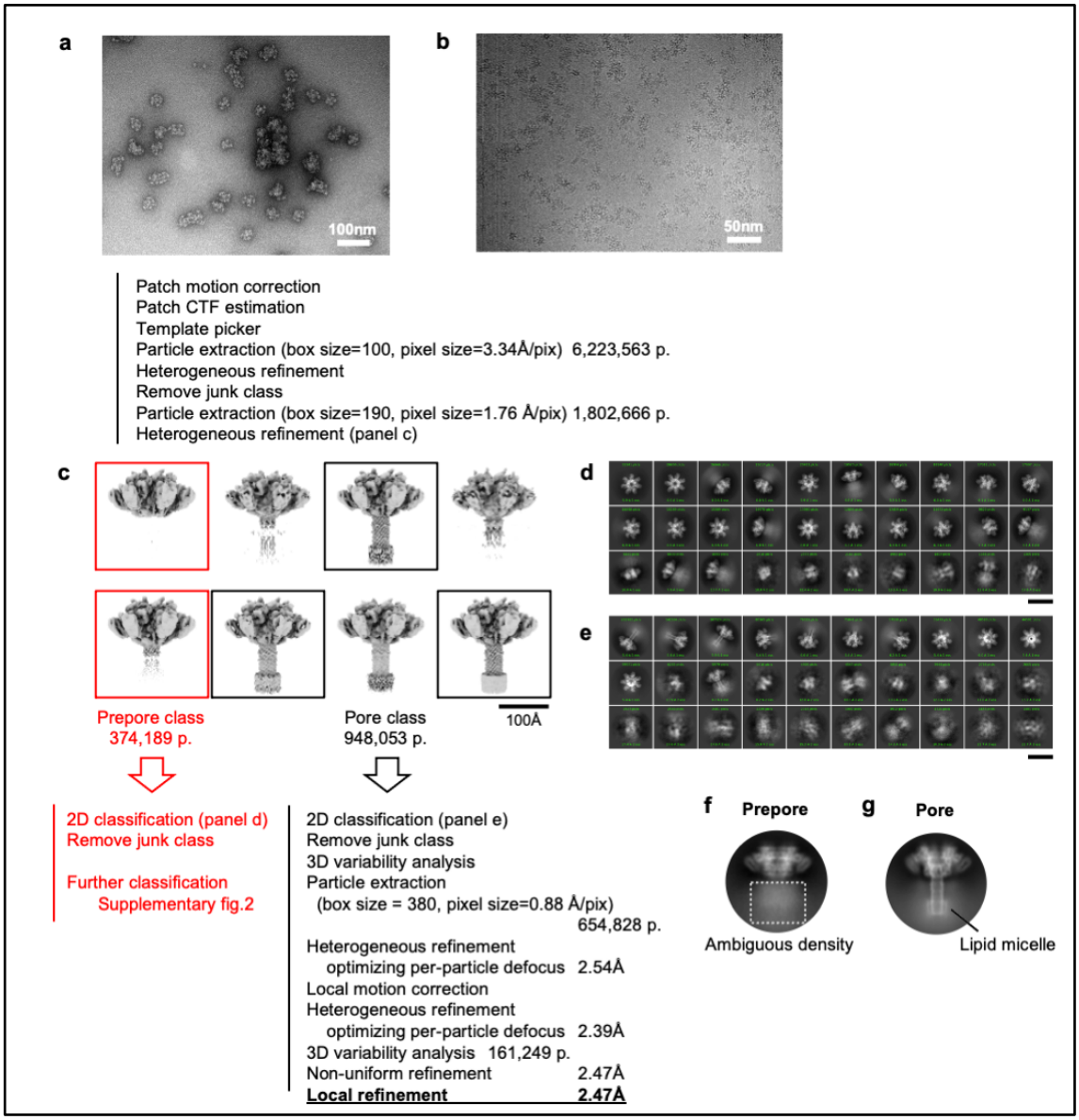

Extended Data Figure 1 | Single particle analysis workflow

a Micrograph of negatively stained Ib-rosette. **b** Cryo-EM micrograph of the Ib-rosette. **c** Representative density maps calculated using heterogeneous refinement. The classes marked with squares were manually sorted into the Ib-prepore particle set (red) and Ib-pore particle set (black). **d, e** Averaged images of Ib-prepores and Ib-pores calculated using 2D classification. The scale bar represents a length of 200 Å. **f, g** Representative 2D average images of the side views of the Ib-prepores and Ib-pores.

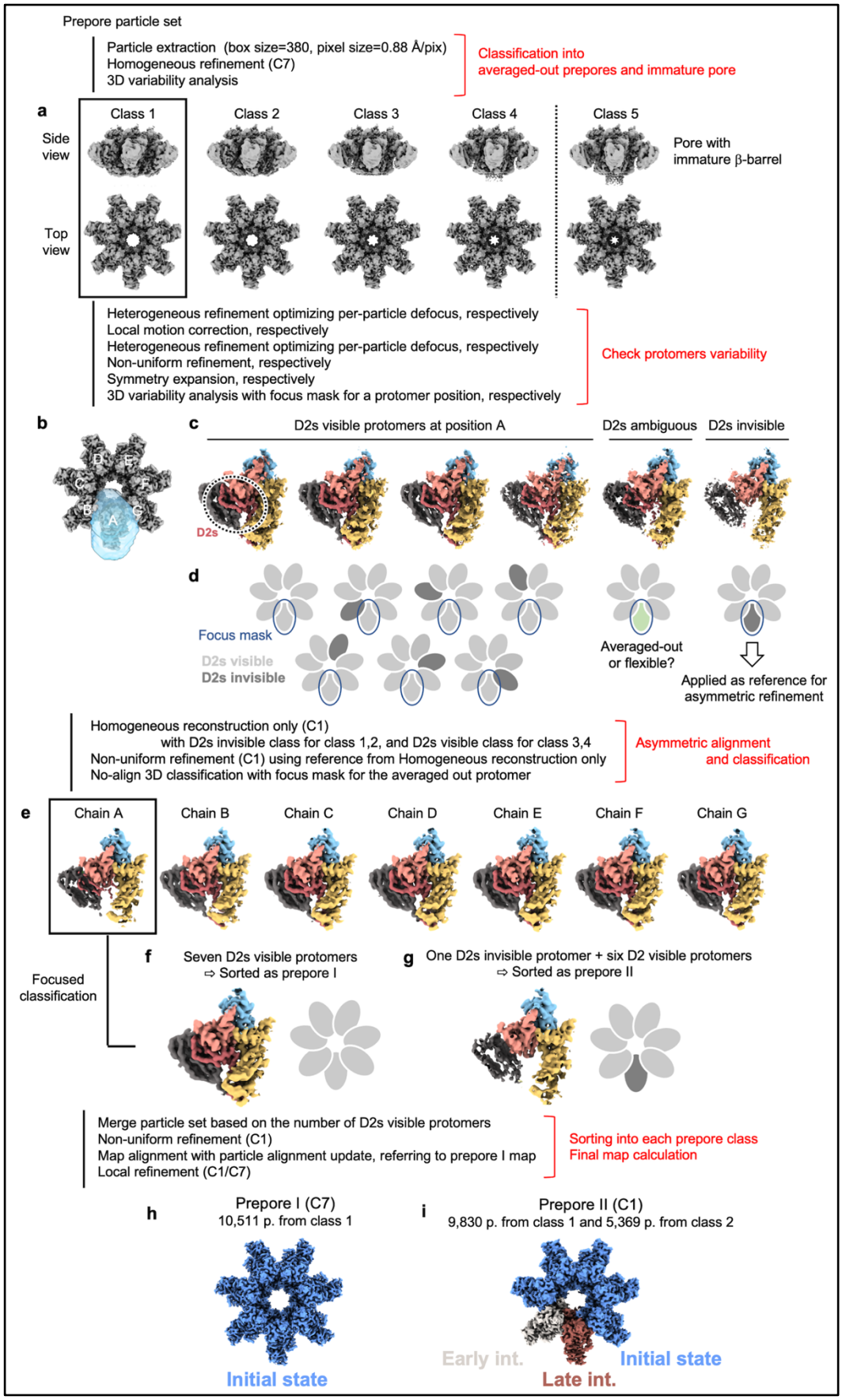
Prepore particle set
Particle extraction (box size=380, pixel size=0.88 Å/pix)
Homogeneous refinement (C7)
3D variability analysis
Classification into
averaged-out prepores and immature pore
a
Class 1
Class 2
Class 3
Class 4
Class 5
Side view
Top view
Pore with
immature β-barrel
Heterogeneous refinement optimizing per-particle defocus, respectively
Local motion correction, respectively
Heterogeneous refinement optimizing per-particle defocus, respectively
Non-uniform refinement, respectively
Symmetry expansion, respectively
3D variability analysis with focus mask for a protomer position, respectively
Check protomers variability
b
c
D2s visible protomers at position A
D2s ambiguous
D2s invisible
D2s
d
Focus mask
D2s visible
D2s invisible
Averaged-out
or flexible?
Applied as reference for
asymmetric refinement
Homogeneous reconstruction only (C1)
with D2s invisible class for class 1,2, and D2s visible class for class 3,4
Non-uniform refinement (C1) using reference from Homogeneous reconstruction only
No-align 3D classification with focus mask for the averaged out protomer
Asymmetric alignment
and classification
e
Chain A
Chain B
Chain C
Chain D
Chain E
Chain F
Chain G
Focused
classification
f
Seven D2s visible protomers
⇨ Sorted as prepore I
g
One D2s invisible protomer + six D2 visible protomers
⇨ Sorted as prepore II
Merge particle set based on the number of D2s visible protomers
Non-uniform refinement (C1)
Map alignment with particle alignment update, referring to prepore I map
Local refinement (C1/C7)
Sorting into each prepore class
Final map calculation
h
Prepore I (C7)
10,511 p. from class 1
i
Prepore II (C1)
9,830 p. from class 1 and 5,369 p. from class 2
Initial state
Early int.
Initial state
Late int.

Extended Data Figure 2 | Detailed classification workflow for Ib-prepore

a Classes obtained from 3D variability analysis. **b** Density of subunit A (transparent light blue) indicates the mask used for focused classification of symmetry-expanded particles. **c, d** Classes obtained from focused 3D variability analysis and the corresponding diagram of the possible relative positions between the focused mask and D2s-visible or D2s-invisible protomers. **e** Protomer maps extracted from the non-uniform refinement output. Subunit A shows a weak D2s density because the D2s-visible protomer (**f**) and the D2s-invisible protomer (**g**) are aligned at the same position. **h, i** Ib-prepore maps obtained from Class 1 particles.

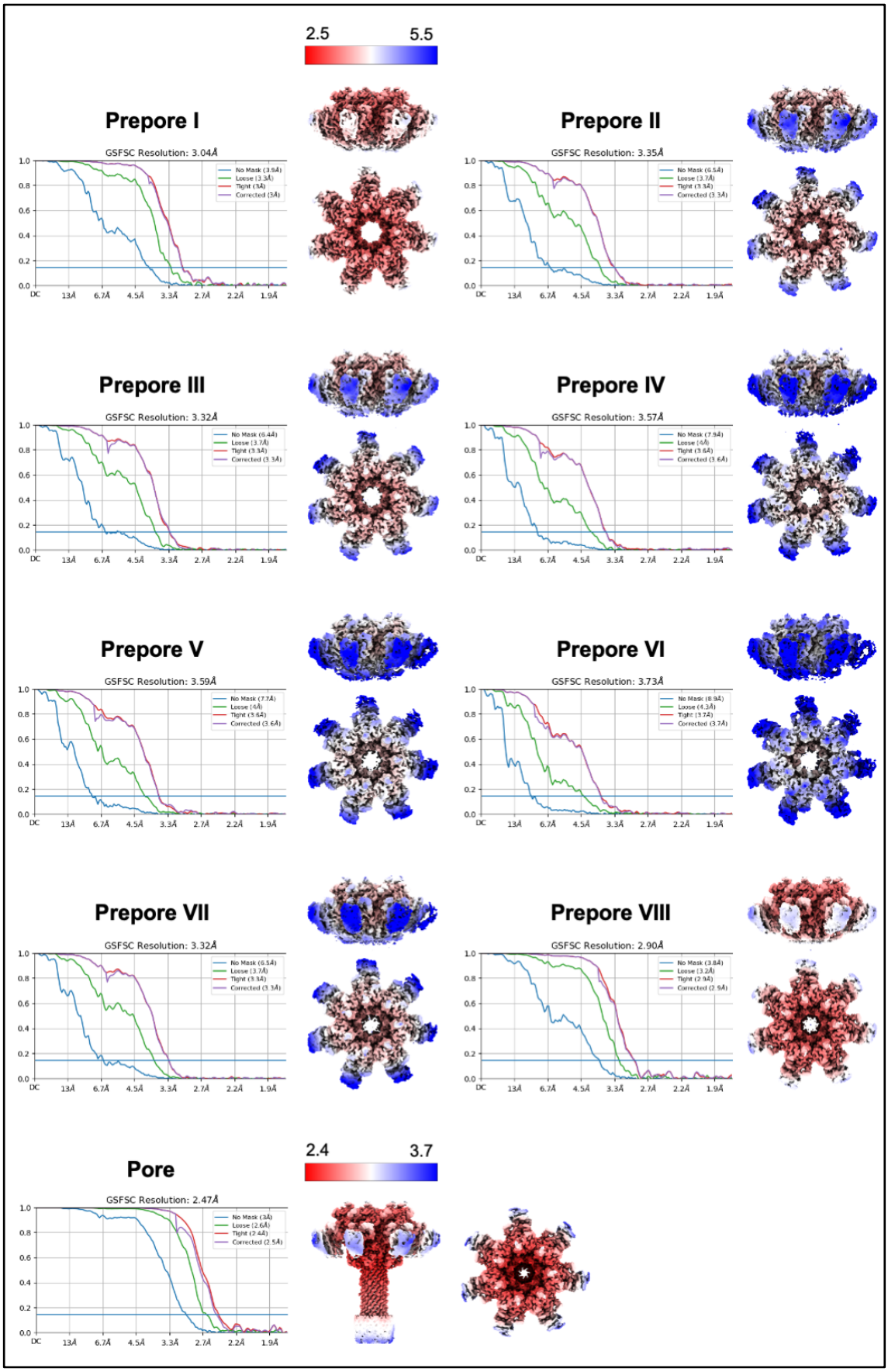
2.5
5.5
Prepore I
GSFSC Resolution: 3.04Å
Prepore II
GSFSC Resolution: 3.35Å
Prepore III
GSFSC Resolution: 3.32Å
Prepore IV
GSFSC Resolution: 3.57Å
Prepore V
GSFSC Resolution: 3.59Å
Prepore VI
GSFSC Resolution: 3.73Å
Prepore VII
GSFSC Resolution: 3.32Å
Prepore VIII
GSFSC Resolution: 2.90Å
Pore
GSFSC Resolution: 2.47Å
2.4
3.7

772

Extended Data Figure 3 | Global and local resolution

The global resolution was calculated using the gold-standard FSC threshold of 0.143. The local resolution was estimated with the RELION Local Resolution job using the final half-maps that are calculated using CryoSPARC. For Ib-prepore, the maps are coloured by the same resolution range (2.5 Å to 5.5 Å), while an independent resolution range coloured Ib-pore due to its outstanding resolution.

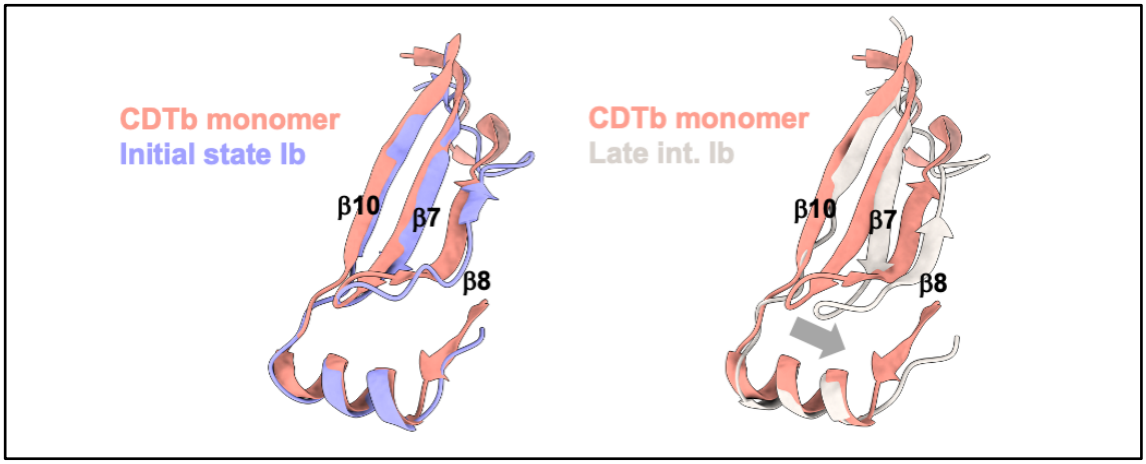

Extended Data Figure 4 | Structural comparison between Ib and CDTb monomer

The monomeric CDTb structure (PDBID: 8DCM) was aligned to the Ib Initial state from Prepore I and the Early int. from Prepore II.

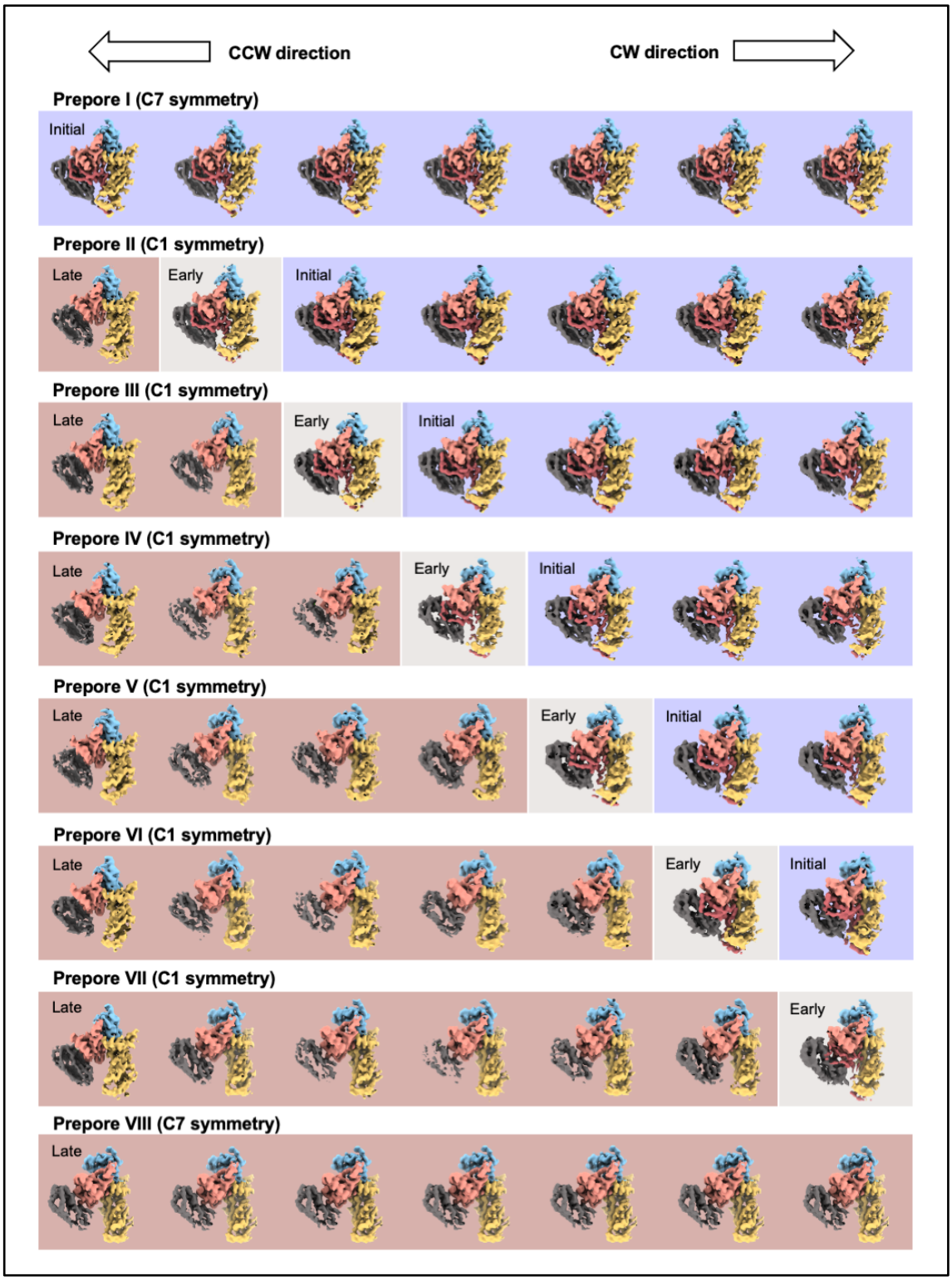

Extended Data Figure 5 | Protomers profile contained in oligomers

Density maps of the protomers were trimmed from their respective prepores, along with their atomic models. Owing to the symmetry for averaging, applied during the single particle analysis, all protomer maps from Prepore I and Prepore VIII are same. The CW and CCW

directions were defined relative to the top of the Ib oligomer where the Ia docking region was located.

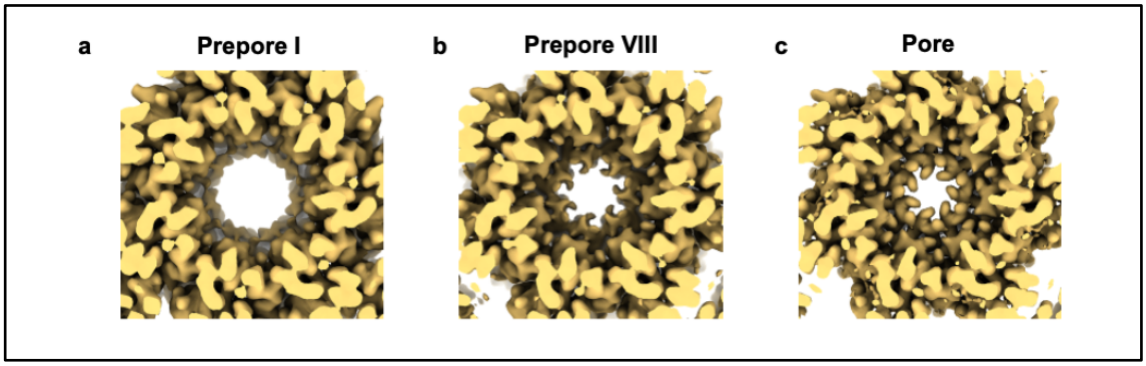

Extended Data Figure 6 | Comparison of the constriction-site top view

A close-up view of the central constriction site. Each map was calculated using C7 symmetry.

Supplementary Movie 1 | Comparison of monomer structures

The atomic models of a protomer in Prepore I, Prepore II, Prepore VIII and the Pore are utilized to represent the Initial, Early int., Late int. and Pore states, respectively.

Supplementary Movie 2 | Structures of interface between the protomers in Initial state–Initial state and protomers in Early int.–Late int.

The movie was created using atomic models and cryo-EM density maps of Prepore I and Prepore II.

Supplementary Movie 3 | Shift in the position of α5 during structural transitions

The video was generated using atomic models arranged to reflect conformational changes propagating in the CW direction. Reverse propagation of the conformational changes in the CCW direction may occur as well.